Journal of Solid State Chemistry 201 (2013) 191–203

Contents lists available at SciVerse ScienceDirect

Journal of Solid State Chemistry

journal homepage: www.elsevier.com/locate/jssc

Rare-earth metal gallium silicides via the gallium self-flux method. Synthesis, crystal structures, and magnetic properties of $RE(Ga_{1-x}Si_x)_2$ (RE=Y, La–Nd, Sm, Gd–Yb, Lu)

Gregory M. Darone [a], Benjamin Hmiel [a], Jiliang Zhang [a], Shanta Saha [b], Kevin Kirshenbaum [b], Richard Greene [b], Johnpierre Paglione [b], Svilen Bobev [a,*]

[a] Department of Chemistry and Biochemistry, University of Delaware, Newark, Delaware 19716, USA
[b] Department of Physics, University of Maryland, College Park, Maryland 20742, USA

ARTICLE INFO

Article history:
Received 11 January 2013
Received in revised form
19 February 2013
Accepted 22 February 2013
Available online 6 March 2013

Keywords:
Rare-earth intermetallics
Flux synthesis
Crystal structure
Magnetic properties
Single-crystal X-ray diffraction

ABSTRACT

Fifteen ternary rare-earth metal gallium silicides have been synthesized using molten Ga as a molten flux. They have been structurally characterized by single-crystal and powder X-ray diffraction to form with three different structures—the early to mid-late rare-earth metals RE=La–Nd, Sm, Gd–Ho, Yb and Y form compounds with empirical formulae $RE(Ga_xSi_{1-x})_2$ ($0.38 \le x \le 0.63$), which crystallize with the tetragonal α-$ThSi_2$ structure type (space group $I4_1/amd$, No. 141; Pearson symbol $tI12$). The compounds of the late rare-earth crystallize with the orthorhombic α-$GdSi_2$ structure type (space group *Imma*, No. 74; Pearson symbol $oI12$), with refined empirical formula $REGa_xSi_{2-x-y}$ (RE=Ho, Er, Tm; $0.33 \le x \le 0.40$, $0.10 \le y \le 0.18$). $LuGa_{0.32(1)}Si_{1.43(1)}$ crystallizes with the orthorhombic $YbMn_{0.17}Si_{1.83}$ structure type (space group *Cmcm*, No. 63; Pearson symbol $oC24$). Structural trends are reviewed and analyzed; the magnetic susceptibilities of the grown single-crystals are presented.

1. Introduction

Although tetragonal α-$ThSi_2$ (own type) and hexagonal β-$ThSi_2$ (AlB_2-type) have been known for some time to be superconductors at 3.2 K and 2.4 K, respectively [1], the discovery of MgB_2 (AlB_2-type) as a high-temperature superconductor at 39 K in 2001 by Nagamatsu et al. [2] spurred renewed interest in the AlB_2 structure type as a source of new materials with interesting properties. Exploration of AlB_2-type ternary aluminum silicides and gallium silicides with alkaline-earth elements proved to be fruitful, with $AE(Ga_xSi_{1-x})_2$ (AE=Ca, Sr, Ba) showing superconductivity with critical temperatures of 3.3 K–3.9 K [3–5], and CaAlSi and SrAlSi at 7.8 K and 5.1 K, respectively [6–10]. With AlB_2-type β-$ThSi_2$ acting as a bridge to the AlB_2-type ternary aluminum and gallium silicides above, expansion to the rare-earth metal aluminum and gallium silicides was a natural progression. Research in the RE–Al–Si system (RE=La, Ce, Nd) done by Raman and Steinfink [11] showed a relationship between the valence electron count in the structure and the progression of structure type $MgCu_2$ to AlB_2 to α-$ThSi_2$ to α-$GdSi_2$; however more recent research by Imai et al. revisited this system suggesting that Si content may also play a role [12]. The RE–Ga–Si systems have been previously explored using arc-melting, producing ternary compounds of both α-$ThSi_2$ and α-$GdSi_2$ structure types [13–20]. Given our lab's history of growth of single-crystals of alkaline-earth and rare-earth metal compounds via Al or Ga self-flux synthesis, such as $Yb_{11}GaSb_9$ [21], $REAl_xSi_{2-x}$ ($x \sim 1$) (RE= La–Nd, Sm, Gd), $RE_2Al_3Si_2$ (RE=Tb–Tm), $REAl_2Si_2$ (RE=Eu, Yb), and LuAlSi [22], $GdCu_4Al$ and $GdCu_4Ga$ [23], $EuAl_{4-x}Si_x$ ($x \sim 1$), and TmAlSi [24], $A_7Ga_2Sb_6$ (A=Sr, Ba, Eu) [25], and $BaGa_2Pn_2$ (Pn=P, As) [26], we embarked on an exploration of the RE–Ga–Si ternary system with the aim to systematically investigate the structural "boundaries" between the α-$ThSi_2$ and α-$GdSi_2$-type structures, and to study the magnetic properties of the newly synthesized single-crystalline materials.

2. Experimental

2.1. Synthesis

Handling of all starting materials was performed inside a dry, argon-atmosphere glovebox or under vacuum. Pure elements were obtained from Ames Lab, Alfa, or Aldrich, with stated purity >99.9%. All metals were used as received; Si was ground into a fine powder before use. Mixtures of the elements with the stoichiometric ratio of 1:7:2 (RE:Ga:Si; total weight ca. 500 mg) were loaded into alumina crucibles, which were then enclosed in evacuated fused silica tubes. The silica-jacketed crucibles were

* Corresponding author. Fax: +1 302 831 6335.
E-mail address: bobev@udel.edu (S. Bobev).

0022-4596/$ - see front matter © 2013 Elsevier Inc. All rights reserved.
http://dx.doi.org/10.1016/j.jssc.2013.02.029

heated using a programmable furnace to 1473 K at a rate of 100 K/h, equilibrated for 24 h, then cooled to 773 K at a rate of 20 K/h. The crucibles were removed from the furnace, inverted, and centrifuged to spin off excess Ga flux. The syntheses were highly reproducible, resulting in silvery plate-like crystals of the title compounds (1–5 mm in length), and easily distinguishable from the unreacted Si. The crystals obtained from different batches had the same morphology/size and virtually identical compositions, confirmed not only by refinements, but also by the property measurements.

Mixtures of the elements with the ratio of 1:7:1 (*RE*:Ga:Si) under the same reaction conditions yielded crystals of REGa$_2$, REGa$_6$, and unreacted Si. Using Ga in excess Ga (as a self-flux), apparently, also required larger than stoichiometric amount of Si. Direct fusion of the elements with the ratio of 1:1:1 *RE*:Ga:Si allows for the formation of the desired REGa$_{1+x}$Si$_{1-x}$ phases, but the powder diffraction patterns of the products suggested some inhomogeneity—this rendered such samples unsuitable for property measurements. In addition, the crystals obtained via this method were of poor quality, which hindered the structural analyses by single-crystal X-ray diffraction.

Attempts at Ga-flux synthesis of EuGaSi produced the readily-formed binary compound EuGa$_4$ [27]. Stoichiometric syntheses in the Eu–Ga–Si system by You et al. [19] succeeded in synthesizing AlB$_2$-type crystals for EuGa$_{1.68}$Si$_{0.32}$ to EuGa$_{0.36}$Si$_{1.64}$ and α-ThSi$_2$-type crystals for EuGa$_{0.36}$Si$_{1.64}$ to EuSi$_2$.

2.2. Powder X-ray diffraction

X-ray powder diffraction patterns were collected at room temperature on a Rigaku MiniFlex powder diffractometer using Cu Kα radiation (λ=1.54056 Å). For each compound, 6–8 crystals were hand-selected and ground together in an agate mortar and pestle; the fine powder was dispersed onto a thin homogenous layer to holder using high-vacuum grease. The observed peak-positions and the peaks' relative intensities, matched well with those calculated from the single-crystal work. Peak widths were small, suggestive that the prepared samples were very homogeneous (see Supporting information). The presence (in some cases) of unindexed peaks suggests that there are yet to be identified compounds in these systems.

Comparison of the powder diffraction patterns collected from specimens preserved in an inert atmosphere and from those exposed to air over several months showed no difference in peak height or position, suggesting the target crystals are not air or moisture sensitive over that time.

2.3. Single-crystal X-ray diffraction

Single-crystal X-ray diffraction data were collected on a Bruker SMART CCD-based diffractometer, employing monochromated Mo Kα radiation (λ=0.71073 Å). For each compound, single-crystals were selected under the microscope, cut to suitable dimensions in Paratone N-Oil, and mounted on the tip of a glass fiber for placement on the goniometer. Samples were cooled to 120 K using a cold nitrogen gas stream. Rapid scans of several crystals were done in case in order to select the highest quality crystal for further analysis. Full spheres of intensity data were gathered in four batch runs with frame width of 0.4 for θ and ω. Data acquisition was controlled by the SMART program [28], and intensities were extracted and corrected for Lorentz and polarization effects using the SAINT program [29]. Semi-empirical absorption corrections were calculated based on equivalents and applied using the SADABS software package [30]. Intensity statistics and space group determination were handled by the subprogram XPREP in the SHELXTL software package [31]. Structures were solved using direct methods and refinement to convergence was done by full matrix least-squares methods on F^2. Refined parameters included the scale factor, the atomic positions with anisotropic displacement parameters, site occupancies, and extinction coefficients (where necessary). In all cases, the intensity statistics $|E^2-1|$ values were consistent with centrosymmetric space groups and all structures were refined in $I4_1/amd$, *Imma*, and *Cmcm*. For a few RE(Ga$_x$Si$_{1-x}$)$_2$ (x=0.5), attempts were made to refine the structures in the non-centrosymmetric space group $I4_1md$, as exemplified by the LaPtSi type. This could allow ordering of Si and Ga, but these refinements did not converge readily, and more importantly—did not provide evidence for ordering.

In the final refinement cycles, atomic positions were standardized using the STRUCTURE TIDY software [32]. Important crystallographic data, atomic positions, displacement parameters, and selected interatomic distances for the series are listed in Tables 1–5. The refined compositions were confirmed by elemental microanalyses (below). Additional details of the crystal structure investigations may be obtained from Fachinformationszentrum Karlsruhe, D-76344 Eggenstein-Leopoldshafen, Germany (Fax: +49-7247-808-666, E-Mail: crysdata@fiz-karlsruhe.de) by quoting the depository numbers CSD-425515 for LaGa$_{0.84}$Si$_{1.16(2)}$, CSD-425516 for CeGa$_{0.87}$Si$_{1.13(1)}$, CSD-425517 for PrGa$_{1.02}$Si$_{0.98(4)}$, CSD-425518 for NdGa$_{1.05}$Si$_{0.95(2)}$, CSD-425519 for SmGa$_{1.01}$Si$_{0.99(1)}$, CSD-425520 for GdGa$_{1.23}$Si$_{0.77(4)}$, CSD-425521 for TbGa$_{1.18}$Si$_{0.82(2)}$, CSD-425522 for DyGa$_{1.24}$Si$_{0.76(4)}$, CSD-425523 for HoGa$_{1.12}$Si$_{0.88(4)}$, CSD-425524 for HoGa$_{0.34(3)}$Si$_{1.56(5)}$, CSD-425525 for ErGa$_{0.41(2)}$Si$_{1.43(4)}$, CSD-425526 for TmGa$_{0.32(2)}$Si$_{1.50(4)}$, CSD-425527 for YbGa$_{0.76}$Si$_{1.24(2)}$, CSD-425528 for LuGa$_{0.32(1)}$Si$_{1.43(1)}$, and CSD-425529 for YGa$_{1.26}$Si$_{0.74(1)}$.

2.4. Energy-dispersive X-ray spectroscopy (EDX) analysis

EDX analysis was conducted using a JEOL 7400F electron microscope equipped with an INCA-Oxford energy-dispersive spectrometer. Data were acquired for several areas on the same crystal and then averaged. The results are in good agreement with the refined compositions and the elemental-maps confirm the homogeneity of the samples.

2.5. Magnetic susceptibility measurements

Magnetization (both field and zero-field cooling) measurements were performed in a Quantum Design MPMS SQUID magnetometer and a Quantum Design PPMS. To ensure reproducibility, specimens from at least two different reaction batches were measured. In all cases, the samples (ca. 20 mg of single-crystal or polycrystalline material) were secured in gel capsules using tape. The raw magnetization data were corrected for the holder contribution and converted to molar susceptibility ($\chi_m=M/H$).

3. Results and discussion

3.1. Structure

The compounds of the early and the mid-late rare-earth elements (RE=La–Nd, Sm, Gd–Ho), plus Yb and Y, crystallize with the tetragonal α-ThSi$_2$ structure type (space group $I4_1/amd$, No. 141; Pearson symbol $tI12$). Their refined empirical formula is RE(Ga$_x$Si$_{1-x}$)$_2$ ($0.38(1)\le x\le 0.63(1)$). The compounds of the late rare-earth crystallize in an orthorhombic variant of this structure, known as the α-GdSi$_2$ structure type (space group *Imma*, No. 74; Pearson symbol $oI12$), with refined empirical formula REGa$_x$Si$_{2-x-y}$ (RE=Ho–Tm; $0.33(2)\le x\le 0.40(2)$, $0.10(5)\le y\le 0.17(4)$). Note the lower Ga

Table 1
Selected single-crystal data collection and structure refinement parameters for tetragonal *RE*GaSi (*RE*=La–Nd, Sm, Gd–Ho, Yb, Y).

Chemical formula	$LaGa_{0.84}Si_{1.16(2)}$	$CeGa_{0.87}Si_{1.13(1)}$	$PrGa_{1.02}Si_{0.98(4)}$	$NdGa_{1.05}Si_{0.95(2)}$
Formula weight, g/mol	230.06	232.69	239.47	244.97
Crystal system		Tetragonal		
Space group, *Z*		$I4_1/amd$, 4		
T, K	120(2)	120(2)	120(2)	120(2)
a, Å	4.3087(16)	4.2426(12)	4.2189(18)	4.1947(9)
c, Å	14.285(11)	14.274(8)	14.296(12)	14.290(6)
V, Å^3	265.2(2)	256.93(17)	254.5(3)	251.45(13)
ρ_{calc}, g/cm^3	5.93	6.15	6.23	6.39
μ(Mo-Kα), cm^{-1}	261.1	280.4	295.7	312.0
Crystal size, mm	0.086 × 0.068 × 0.024	0.087 × 0.054 × 0.053	0.063 × 0.035 × 0.028	0.082 × 0.053 × 0.044
Reflections collected	1228	1255	1152	1207
Independent reflections	105	102	100	99
Goodness-of-fit	1.442	1.219	1.415	1.154
R_1 (I > 2$\sigma_{(I)}$)[a]	0.0316	0.0128	0.0425	0.0180
wR_2 (I > 2$\sigma_{(I)}$)[a]	0.0809	0.0252	0.1020	0.0422
R_1 (all data)[a]	0.0340	0.0163	0.0459	0.0195
wR_2 (all data)[a]	0.0824	0.0261	0.1043	0.0433
Largest peak and hole, e$^-$ · Å^{-3}	1.36; −2.20	0.670; −0.61	1.85; −3.18	1.14; −1.66
Chemical formula	$SmGa_{1.01}Si_{0.99(1)}$	$GdGa_{1.23}Si_{0.77(4)}$	$TbGa_{1.18}Si_{0.82(2)}$	$DyGa_{1.24}Si_{0.76(4)}$
Formula weight, g/mol	248.59	264.64	263.81	271.13
Crystal system		Tetragonal		
Space group, *Z*		$I4_1/amd$, 4		
T, K	120(2)	120(2)	120(2)	120(2)
a, Å	4.1405(3)	4.1298(9)	4.090(2)	4.0811(3)
c, Å	14.209(2)	14.304(6)	14.222(14)	14.2307(17)
V, Å^3	243.60(5)	243.96(12)	237.9(3)	237.02(4)
ρ_{calc}, g/cm^3	6.78	7.21	7.36	7.59
μ(Mo-Kα), cm^{-1}	351.2	404.8	426.7	427.1
Crystal size, mm	0.052 × 0.040 × 0.030	0.084 × 0.064 × 0.041	0.066 × 0.046 × 0.029	0.095 × 0.087 × 0.030
Reflections collected	1228	1208	1117	1145
Independent reflections	98	102	98	97
Goodness-of-fit	1.299	1.309	1.194	1.238
R_1 (I > 2$\sigma_{(I)}$)[a]	0.0118	0.0328	0.0161	0.0278
wR_2 (I > 2$\sigma_{(I)}$)[a]	0.0239	0.0684	0.0360	0.0602
R_1 (all data)[a]	0.0144	0.0341	0.0183	0.0292
wR_2 (all data)[a]	0.0248	0.0698	0.0369	0.0611
Largest peak and hole, e$^-$ · Å^{-3}	0.70; −0.78	2.45; −3.34	1.06; −1.00	1.06; −4.31
Chemical formula	$HoGa_{1.12}Si_{0.88(4)}$	$YGa_{1.26}Si_{0.74(1)}$	$YbGa_{0.88}Si_{1.12(2)}$	
Formula weight, g/mol	267.94	197.71	265.65	–
Crystal system		Tetragonal		–
Space group, *Z*		$I4_1/amd$, 4		–
T, K	120(2)	120(2)	120(2)	–
a, Å	4.0658(9)	4.0935(4)	4.0957(5)	–
c, Å	14.247(6)	14.255(3)	14.220(4)	–
V, Å^3	235.51(12)	238.87(6)	238.53(7)	–
ρ_{calc}, g/cm^3	7.56	5.49	7.40	–
μ(Mo-Kα), cm^{-1}	461.9	382.6	490.1	–
Crystal size, mm	0.072 × 0.066 × 0.030	0.112 × 0.065 × 0.040	0.047 × 0.044 × 0.030	–
Reflections collected	1254	1493	1175	–
Independent reflections	97	98	98	–
Goodness-of-fit	1.207	1.205	1.285	–
R_1 (I > 2$\sigma_{(I)}$)[a]	0.0269	0.0312	0.0153	–
wR_2 (I > 2$\sigma_{(I)}$)[a]	0.0641	0.0647	0.0304	–
R_1 (all data)[a]	0.0300	0.0341	0.0169	–
wR_2 (all data)[a]	0.0657	0.0665	0.0307	–
Largest peak and hole, e$^-$ · Å^{-3}	4.59; −1.14	1.01; −1.92	0.70; −1.18	–

[a] $R_1=\sum||F_o|-|F_c||/\sum|F_o|$; $wR_2=[\sum[w(F_o^2-F_c^2)^2]/\sum[w(F_o^2)^2]]^{1/2}$, where $w=1/[\sigma^2F_o^2+(A\times P)^2+(B\times P)]$, and $P=(F_o^2+2F_c^2)/3$; *A* and *B* – weight coefficients.

content and the presence of vacancies in this structure; the existence of two structures with Ho must also be pointed out and will be discussed further later on. We also specifically mention YbGaSi here—although Yb is the second to last element in the lanthanide block, in this compound Yb is found as Yb^{2+} (diamagnetic [Xe]$4f^{14}$ configuration, as confirmed by the magnetization measurements), whereas all other rare-earth metals exhibited the typical magnetism of the RE^{3+} ions (vide infra). The compound with Lu crystallize with the orthorhombic $YbMn_{0.17}Si_{1.83}$ structure type (space group *Cmcm*, No. 63; Pearson symbol *oC*24); the refined empirical formula is also sub-stoichiometric, $LuGa_{0.32(1)}Si_{1.43(1)}$. For simplicity of notation the title compounds shall be referred to

Table 2
Selected single-crystal data collection and structure refinement parameters for orthorhombic *RE*GaSi (*RE*=Ho–Tm, Lu).

Chemical formula	$HoGa_{0.34(3)}Si_{1.56(5)}$	$ErGa_{0.41(2)}Si_{1.43(4)}$	$TmGa_{0.32(2)}Si_{1.50(4)}$	$LuGa_{0.32(1)}Si_{1.43(1)}$
Formula weight, g/mol	232.48	236.50	233.84	237.49
Crystal system		Orthorhombic		
Space group, *Z*		*Imma*, 4		*Cmcm*, 8
T, K	120(2)	120(2)	120(2)	120(2)
a, Å	3.970(2)	3.9653(16)	3.9283(18)	3.9678(10)
b, Å	4.020(2)	4.0213(16)	3.9961(18)	28.479(7)
c, Å	13.401(7)	13.424(5)	13.308(6)	3.8138(10)
V, Å^3	213.9(2)	214.06(15)	208.90(16)	430.95(19)
ρ_{calc}, g/cm^3	7.19	7.34	7.41	7.31
μ(Mo-Kα), cm^{-1}	414.4	446.3	469.2	499.5
Crystal size, mm	0.052 × 0.040 × 0.033	0.084 × 0.072 × 0.057	0.037 × 0.027 × 0.010	0.024 × 0.024 × 0.011
Reflections collected	1450	1439	916	2754
Independent reflections	173	173	170	349
Goodness-of-fit	1.104	1.081	1.108	1.0435
R_1 ($I > 2\sigma_{(I)}$)[a]	0.0336	0.0266	0.0305	0.0241
wR_2 ($I > 2\sigma_{(I)}$)[a]	0.0890	0.0712	0.0711	0.0517
R_1 (all data)[a]	0.0353	0.0277	0.0359	0.0323
wR_2 (all data)[a]	0.0899	0.0716	0.0737	0.0561
Largest peak and hole/ e$^-\cdot$Å^{-3}	4.45; −2.16	2.63; −2.70	3.11; −2.26	2.35; −1.81

[a] $R_1=\sum||F_o|-|F_c||/\sum|F_o|$; $wR_2=[\sum[w(F_o^2-F_c^2)^2]/\sum[w(F_o^2)^2]]^{1/2}$, where $w=1/[\sigma^2F_o^2+(A\times P)^2+(B\times P)]$, and $P=(F_o^2+2F_c^2)/3$; *A* and *B* – weight coefficients.

Table 3
Refined atomic coordinates, equivalent isotropic displacement parameters (U_{eq}[a]), and occupancy values for tetragonal *RE*GaSi (*RE*=La–Nd, Sm, Gd–Ho, Yb, Y).

Compound	Atom	Wyckoff site	*x*	*y*	*z*	U_{eq}, Å^2	Occupancy
$LaGa_{0.84}Si_{1.16}$	La	4*a*	0	3/4	1/8	0.0077(7)	1
	Ga	8*e*	0	1/4	0.2913(2)	0.009(1)	0.42(1)
	Si	8*e*	0	1/4	0.2913(2)	0.009(1)	0.58(1)
$CeGa_{0.87}Si_{1.13}$	Ce	4*a*	0	3/4	1/8	0.0064(2)	1
	Ga	8*e*	0	1/4	0.29148(6)	0.0075(4)	0.437(5)
	Si	8*e*	0	1/4	0.29148(6)	0.0075(4)	0.563(5)
$PrGa_{1.02}Si_{0.98}$	Pr	4*a*	0	3/4	1/8	0.0087(9)	1
	Ga	8*e*	0	1/4	0.2916(2)	0.010(1)	0.51(2)
	Si	8*e*	0	1/4	0.2916(2)	0.010(1)	0.49(2)
$NdGa_{1.05}Si_{0.95}$	Nd	4*a*	0	3/4	1/8	0.0056(4)	1
	Ga	8*e*	0	1/4	0.29178(8)	0.0073(6)	0.526(9)
	Si	8*e*	0	1/4	0.29178(8)	0.0073(6)	0.474(9)
$SmGa_{1.01}Si_{0.99}$	Sm	4*a*	0	3/4	1/8	0.0030(3)	1
	Ga	8*e*	0	1/4	0.29182(6)	0.0041(4)	0.505(6)
	Si	8*e*	0	1/4	0.29182(6)	0.0041(4)	0.495(6)
$GdGa_{1.23}Si_{0.77}$	Gd	4*a*	0	3/4	1/8	0.0049(8)	1
	Ga	8*e*	0	1/4	0.2920(1)	0.006(1)	0.62(2)
	Si	8*e*	0	1/4	0.2920(1)	0.006(1)	0.38(2)
$TbGa_{1.18}Si_{0.82}$	Tb	4*a*	0	3/4	1/8	0.0054(4)	1
	Ga	8*e*	0	1/4	0.29216(8)	0.0070(6)	0.59(1)
	Si	8*e*	0	1/4	0.29216(8)	0.0070(6)	0.41(1)
$DyGa_{1.24}Si_{0.76}$	Dy	4*a*	0	3/4	1/8	0.0049(7)	1
	Ga	8*e*	0	1/4	0.2923(1)	0.007(1)	0.62(2)
	Si	8*e*	0	1/4	0.2923(1)	0.007(1)	0.38(2)
$HoGa_{1.12}Si_{0.88}$	Ho	4*a*	0	3/4	1/8	0.0064(5)	1
	Ga	8*e*	0	1/4	0.2924(2)	0.007(1)	0.56(2)
	Si	8*e*	0	1/4	0.2924(2)	0.007(1)	0.44(2)
$YbGa_{0.76}Si_{1.24}$	Yb	4*a*	0	3/4	1/8	0.0078(3)	1
	Ga	8*e*	0	1/4	0.2921(1)	0.0151(7)	038(1)
	Si	8*e*	0	1/4	0.2921(1)	0.0151(7)	0.62(1)
$YGa_{1.26}Si_{0.74}$	Y	4*a*	0	3/4	1/8	0.0057(5)	1
	Ga	8*e*	0	1/4	0.29228(6)	0.0073(5)	0.632(5)
	Si	8*e*	0	1/4	0.29228(6)	0.0073(5)	0.368(5)

[a] U_{eq} is defined as one third of the trace of the orthogonalized U_{ij} tensor.

simply as *RE*GaSi for the remainder of this paper, despite the differences in their refined empirical formulas, unless necessary for clarity.

In the tetragonal α-$ThSi_2$-type crystal structures $RE(Ga_xSi_{1-x})_2$ (*RE*=La-Nd, Sm, Gd-Ho, Yb, Y; $0.38(1)\le x\le 0.63(1)$), the lattice parameters ranged from a=4.0658(9) Å—4.3087(16) Å; c=14.209(2) Å—14.285(11) Å; and V=235.51(12) Å^3—265.2(2) Å^3. The trend from larger to smaller unit cells across the series echoes the lanthanide contraction (r_{La}=1.690 Å to r_{Ho}=1.581 Å) [33]. The Ga:Si ratio of the structure also affects the unit cell parameters, due to the difference in radii of Ga and Si (r_{Ga}=1.246 Å and r_{Si}=1.173 Å) [33]. The crystal structure for these compounds is well-known and does not need additional description. We just recall that the *RE* atoms in this structure form trigonal prisms arranged into layers in the *ab* plane. The layers are stacked in an alternating fashion in the *c* direction, as shown in Fig. 1. The mixed-occupied Ga/Si atoms occupy the centers of these trigonal prismatic units, with each Ga/Si atom coordinated by 6 *RE* atoms. Then again, the structure can be described as a polyanionic network of Ga/Si atoms, made up of rectangular prisms, capped with triangular prisms on both ends in the *c* direction, in which the caps are orthogonal to each other. The *RE*-atoms occupy the centers of these 12-vertex polyhedra. These are face-shared and fill the matrix. These two descriptions serve to highlight the dual effects the size of the *RE* element (in the case of the *RE* trigonal prisms) and the Ga:Si ratio (in the case of the Ga/Si atom octahedra) in the unit cell parameters and crystal structure.

In the orthorhombic α-$GdSi_2$-type crystal structures ($REGa_xSi_{2-x-y}$ (*RE*=Ho–Tm; $0.33(2)\le x\le 0.40(2)$, $0.10(5)\le y\le 0.18(4)$)) the lattice parameters range from a=3.9283(18) Å—3.970(2) Å; b=3.9961(18) Å—4.0213(16) Å; c=13.308(6) Å—13.424(5) Å; and V=208.90(16) Å^3—214.06(15) Å^3. The much smaller variance in lattice parameters can be attributed to the very similar chemical compositions, as well as the close radii for Ho, Er, and Tm (r_{Ho}=1.581 Å, r_{Er}=1.580 Å, r_{Tm}=1.578 Å) [33]. The atomic arrangements for these compounds are similar to those of the α-$ThSi_2$-type compounds, except that for the polyanionic framework, the Ga/Si building blocks are composed of randomly mixed occupied Ga/Si atoms (Ga1/Si1 position) for one six-member trigonal prismatic cap, and composed of Si only atoms (Si2 position) for the opposite side cap, as shown in Fig. 2. Again, the *RE* metal atoms are 12-coordinated and occupy the centers of these less-regular polyhedra, which are face-shared as well, but join like-cap to like-cap, with Ga1/Si1 atom ends sharing faces with Ga1/Si1 atom ends, and with Si2 atom ends sharing faces with Si2 atom ends. This gives the matrix alternating corrugated layers, stacked in the *c* direction, of Ga1/Si1 atom bonding environments and Si2 atom bonding environments extending in the *ab* plane. The difference in average bond

Table 4
Refined atomic coordinates, equivalent isotropic displacement parameters (U_{eq}[a]), and occupancy values for orthorhombic *RE*GaSi (*RE*=Ho–Tm, Lu).

Compound	Atom	Wyckoff site	*x*	*y*	*z*	U_{eq}, Å^2	Occupancy
$HoGa_{0.34}Si_{1.56}$	Ho	4*e*	0	1/4	0.6249(1)	0.014(1)	1
	Ga1	4*e*	0	1/4	0.0485(4)	0.025(2)	0.34(3)
	Si1	4*e*	0	1/4	0.0485(4)	0.025(2)	0.66(3)
	Si2[b]	4*e*	0.05(1)	1/4	0.2191(8)	0.056(5)	0.45(5)
$ErGa_{0.41}Si_{1.43}$	Er	4*e*	0	1/4	0.6255(1)	0.012(1)	1
	Ga1	4*e*	0	1/4	0.0491(3)	0.021(1)	0.41(2)
	Si1	4*e*	0	1/4	0.0491(3)	0.021(1)	0.59(2)
	Si2[b]	8*i*	0.054(8)	1/4	0.2196(7)	0.057(9)	0.43(3)
$TmGa_{0.32}Si_{1.50}$	Tm	4*e*	0	1/4	0.6249(1)	0.011(1)	1
	Ga1	4*e*	0	1/4	0.0499(4)	0.018(1)	0.32(2)
	Si1	4*e*	0	1/4	0.0499(4)	0.018(1)	0.68(2)
	Si2[b]	4*e*	0.080(9)	1/4	0.2227(8)	0.06(1)	0.40(3)
$LuGa_{0.32}Si_{1.43}$	Lu1	4*c*	0	0.4399(1)	1/4	0.009(1)	1
	Lu2	4*c*	0	0.6718(1)	1/4	0.009(1)	1
	Ga1	4*c*	0	0.0116(2)	1/4	0.051(6)	0.29(2)
	Si1	4*c*	0	0.0116(2)	1/4	0.051(6)	0.21(2)
	Ga2	4*c*	0	0.0932(2)	1/4	0.007(1)	0.31(1)
	Si2	4*c*	0	0.0932(2)	1/4	0.007(1)	0.19(1)
	Ga3	4*c*	0	0.2490(2)	1/4	0.032(2)	0.06(1)
	Si3	4*c*	0	0.2490(2)	1/4	0.032(2)	0.94(1)
	Ga4	4*c*	0	0.7778(3)	1/4	0.009(3)	0.02(1)
	Si4	4*c*	0	0.7778(3)	1/4	0.009(3)	0.48(1)
	Ga5	4*c*	0	0.8551(2)	1/4	0.014(2)	0.07(2)
	Si5	4*c*	0	0.8551(2)	1/4	0.014(2)	0.93(2)

[a] U_{eq} is defined as one third of the trace of the orthogonalized U_{ij} tensor.
[b] Site 4*e* moved "off-center" to a 50% occupied 8*i* site.

distance for the Ga1/Si1 layers versus the Si2 layers causes distortion of the octahedral building blocks, as the two ends are not symmetrical. This distortion cannot extend throughout the crystal matrix, however, because the polyanionic framework fills the matrix completely. To compensate for this distortion, vacancies in the Si2 atom position exist, typically exhibiting only 82(4)%–90(5)% occupancy in our refinements. These vacancies allow for periodic "readjustment" of the Si/Ga sub-structure, as the Si2 atom positions adjacent to the vacancy are afforded more room to move to positions more symmetrical to the Ga1/Si1 layer. This variable position for the Si2 atom results in an abnormally high anisotropic displacement parameter in the *a* direction in refinements. For comparison, the anisotropic displacement parameters for the Si2 position in ErGaSi were refined as: $U_{11}=0.14(1)$, $U_{22}=0.015(4)$, $U_{33}=0.018(5)$, while refinements for the Ga/Si mixed occupied site in tetragonal SmGaSi they were $U_{11}=0.0025(6)$, $U_{22}=0.0064(6)$, $U_{33}=0.0034(6)$. The unphysical Si2–Si2 distances (Table 3), shorter than the sum of the single-bonded Si radii can be attributed to the Si2 vacancies and the positional disorder in the Si2 chains.

Our experiments with Lu did not produce α-$GdSi_2$-type crystals like the other late rare-earth metals, but instead produced $LuGa_{0.32(1)}Si_{1.43(1)}$, which crystallizes with the orthorhombic $YbMn_{0.17}Si_{1.83}$ structure type (space group *Cmcm*). The framework for this structure can be imagined as an intergrowth of three layers of AlB_2-like units sandwiched between two layers of $BaAl_4$-like units [34]. In the AlB_2-like units, the Lu atoms occupy the Al positions, to form a framework of fused trigonal prisms, with Ga/Si atoms occupying B positions at their centers. In these trigonal prisms, two of the unique Ga/Si atom positions, Ga1/Si1 and Ga2/Si2, refine with 50% occupancy, while the third unique Ga/Si position, Ga5/Si5, refines with full occupancy. The $BaAl_4$-like units "bookend" the AlB_2-like layers, stacked above and below in the *b* direction. This layer can be described as a puckered net of mixed occupancy Ga/Si atoms. Of the two unique atom sites in the layer, the Ga3/Si3 position is refined with full occupancy, while the Ga4/Si4 position is refined with a combined 50% occupancy. Alternatively, the structure can be imagined as a polyanionic network of Ga/Si atoms, forming face-sharing octahedra sandwiched between the Ga/Si puckered nets. These two representations are schematically shown in Fig. 3.

3.2. Chemical bonding and the relationship between rare-earth metal size and structure

RE-Ga/Si distances in the α-$ThSi_2$-type tetragonal crystal structures (*RE*=La–Nd, Sm, Gd–Ho, Yb, Y) range from 3.1067(11) Å—3.2732(14) Å. Ga/Si–Ga/Si distances range from 2.355(5) Å—2.456(2) Å. These values are similar to the Ga–Si distances of 2.39 Å—2.47 Å seen in CaGaSi, SrGaSi, and BaGaSi [35] and the distances of 2.511(5) Å—2.597(5) Å seen in $Gd_5Ga_{0.99}Si_{3.01}$ [36].

RE–Ga/Si distances in the α-$GdSi_2$-type orthorhombic crystal structures (*RE*=Ho–Tm) range from 2.863(8) Å—3.133(2) Å. Ga/Si–Ga/Si distances range from 2.398(6) Å—2.400(5) Å. The partial occupancy and positional disorder of the Si2 atom positions result in Si2–Si2 distances that are too short, ranging from 2.110(8) Å—2.168(8) Å. This phenomenon was also reported in the Si–Si distances (2.13(5) Å—2.21(3) Å) for the orthorhombic structure in $GdSi_{1.85}$ [37].

Lu–Ga/Si distances in the orthorhombic crystal structure $LuGa_{0.32(1)}Si_{1.43(1)}$ range from 2.844(5) Å—3.127(4) Å. These are slightly longer than the range of Lu–Si distances of 2.842(3) Å—2.980(4) Å reported for LuAlSi by Tobash et al. [24]. Ga/Si–Ga/Si distances range from 2.016(5) Å—2.7524(6) Å. The unusually long and short distances highlight the distortion of the $BaAl_4$-unit puckered nets and misshapen AlB_2-like pieces of the structure, as well as the vacancies in three of the five Ga/Si positions.

Crystal structure variations across the series for rare-earth metal disilicides and digermanides are known to be due to the interplay between the decreasing atomic sizes of the lanthanides with increased *Z*-number, variable stoichiometry, etc. Polymorphic transitions as functions of the temperature have been studied extensively by others as well [38–44]. Murashita et al. [38] explored the role of stoichiometry and temperature in the crystal structure of $CeSi_{2-x}$, noting that the structure changed from α-$ThSi_2$ to α-$GdSi_2$ when $x>0.3$. Furthermore, at low

Table 5
Selected interatomic distances (Å).

$LaGa_{0.84}Si_{1.16}$	La–	Ga/Si × 8	3.206(2)
		Ga/Si × 8	3.273(1)
	Ga/Si–	Ga/Si × 2	2.393(5)
		Ga/Si × 4	2.456(2)
$CeGa_{0.87}Si_{1.13}$	Ce–	Ga/Si × 8	3.185(1)
		Ga/Si × 8	3.2282(9)
	Ga/Si–	Ga/Si × 2	2.384(2)
		Ga/Si × 4	2.429(1)
$PrGa_{1.02}Si_{0.98}$	Pr–	Ga/Si × 8	3.182(3)
		Ga/Si × 8	3.213(2)
	Ga/Si–	Ga/Si × 2	2.385(6)
		Ga/Si × 4	2.422(3)
$NdGa_{1.05}Si_{0.95}$	Nd–	Ga/Si × 8	3.175(1)
		Ga/Si × 8	3.1956(7)
	Ga/Si–	Ga/Si × 2	2.378(2)
		Ga/Si × 4	2.414(1)
$SmGa_{1.01}Si_{0.99}$	Sm–	Ga/Si × 8	3.1473(7)
		Ga/Si × 8	3.1573(4)
	Ga/Si–	Ga/Si × 2	2.364(2)
		Ga/Si × 4	2.3872(9)
$GdGa_{1.23}Si_{0.77}$	Gd–	Ga/Si × 8	3.1522(9)
		Ga/Si × 8	3.158(2)
	Ga/Si–	Ga/Si × 2	2.374(4)
		Ga/Si × 4	2.389(2)
$TbGa_{1.18}Si_{0.82}$	Tb–	Ga/Si × 8	3.123(1)
		Ga/Si × 8	3.136(2)
	Ga/Si–	Ga/Si × 2	2.356(3)
		Ga/Si × 4	2.371(2)
$DyGa_{1.24}Si_{0.76}$	Dy–	Ga/Si × 8	3.1163(7)
		Ga/Si × 8	3.136(1)
	Ga/Si–	Ga/Si × 2	2.353(4)
		Ga/Si × 4	2.370(2)
$HoGa_{1.12}Si_{0.88}$	Ho–	Ga/Si × 8	3.107(1)
		Ga/Si × 8	3.133(2)
	Ga/Si–	Ga/Si × 2	2.355(5)
		Ga/Si × 4	2.364(2)
$YbGa_{0.76}Si_{1.24}$	Yb–	Ga/Si × 8	3.1269(6)
		Ga/Si × 8	3.137(1)
	Ga/Si–	Ga/Si × 2	2.358(2)
		Ga/Si × 4	2.372(1)
$YGa_{1.26}Si_{0.74}$	Y–	Ga/Si × 8	3.1255(4)
		Ga/Si × 8	3.1426(7)
	Ga/Si–	Ga/Si × 2	2.358(2)
		Ga/Si × 4	2.3754(8)
$HoGa_{0.34}Si_{1.56}$	Ho–	Ga1/Si1 × 12	3.107(1)
		Ga1/Si1 × 4	3.133(2)
		Si2 × 4	2.913(8)
		Si2 × 4	3.087(5)
	Ga1/Si1–	Si2 × 2	2.27(1)
		Ga1/Si1 × 4	2.390(7)
	Si2–	Si2 × 2	2.165(9)
$ErGa_{0.40}Si_{1.46}$	Er–	Ga1/Si1 × 12	3.005(2)
		Ga1/Si1 × 4	3.067(4)
		Si2 × 4	2.915(7)
		Si2 × 4	3.081(4)
	Ga1/Si1–	Si2 × 2	2.26(1)
		Ga1/Si1 × 4	2.400(5)
	Si2–	Si2 × 2	2.168(8)
$TmGa_{0.33}Si_{1.50}$	Tm–	Ga1/Si1 × 12	2.975(2)
		Ga1/Si1 × 4	3.043(4)
		Si2 × 4	2.863(8)
		Si2 × 4	3.080(5)
	Ga1/Si1–	Si2 × 2	2.28(1)
		Ga1/Si1 × 4	2.398(6)
	Si2–	Si2 × 2	2.110(8)
$LuGa_{0.32}Si_{1.43}$	Lu1–	Ga1/Si1 × 6	2.844(5)
		Ga1/Si1 × 4	3.080(3)
		Ga2/Si2 × 12	2.908(2)
		Ga5/Si5 × 2	3.127(4)
	Lu2–	Ga2/Si2 × 2	2.992(4)
		Ga3/Si3 × 4	2.954(4)
		Ga4/Si4	3.011(9)
		Ga4/Si4	3.107(4)
		Ga5/Si5 × 12	2.856(2)
	Ga1/Si1–	Ga1/Si1 × 4	2.016(5)
		Ga2/Si2	2.326(9)
	Ga2/Si2–	Ga5/Si5 × 8	2.411(4)
	Ga3/Si3–	Ga3/Si3 × 4	2.7524(6)
		Ga4/Si4 × 8	2.051(4)
		Ga4/Si4 × 8	2.144(4)
	Ga5/Si5–	Ga4/Si4	2.21(1)

temperatures, both structures experienced a non-linear reduction in the *c* lattice parameter, and there was an emergence of a second low-temperature crystal structure that better utilizes the Si vacancies with the structure's free energy potential. Houssay et al. investigated the role of the rare-earth element in the rare-earth disilicides, observing that the early rare-earth elements (*RE*=La–Pr) adopted the α-$ThSi_2$ or α-$GdSi_2$ structure types, the mid rare-earths (*RE*=Nd, Gd) adopted the α-$GdSi_2$ or AlB_2 structure types, and the late rare-earths (*RE*=Er, Yb) adopted only the AlB_2 structure type [39]. Souptel et al. [40] further investigated the $CeSi_{2-x}$ system, developing a binary phase diagram for both the formation temperatures and composition windows of α-$ThSi_2$ and α-$GdSi_2$-type $CeSi_{2-x}$. Of particular interest was the observation that the α-$GdSi_2$-type formed at higher temperatures than the α-$ThSi_2$-type. Bulanova et al. observed similar temperature distinctions in their investigation of the $LaSi_{2-x}$ and $CeSi_{2-x}$ compounds [41,42].

Considering the *RE*GaSi compounds of this paper as disilicides with gallium substitution allows for direct comparison with these previous findings. We remind the reader again that our syntheses involved a stoichiometric excess of both Ga and Si (see Section 2). Thus, the structure determination factors are believed to be the atom sizes (a combination of the lanthanide contraction and an increase of the "Si atom size" due to the substitution by the larger Ga) and the temperature. Adapting Houssay's conclusions, we see a division of the early to mid rare-earth elements (*RE*=La–Nd, Sm, Gd–Ho, Yb, Y) adopting the α-$ThSi_2$ structure, while the late rare-earth elements (*RE*=Ho–Tm) adopted the α-$GdSi_2$ structure type. Lu adopted the $YbMn_{0.17}Si_{1.83}$ structure type, which with its three layers of AlB_2 topology and one $BaAl_4$ unit can be seen as a progression from the α-$GdSi_2$-type toward a relative of the AlB_2-type. Due to the severe disorder, the presented herein refinement may not the final word on the LuGaSi structure determination—one could imagine multiple superstructures with full or partial ordering, evidence for which is not currently available.

The logical conclusion is that the inclusion of gallium in the structures shifted these divisions further down the series than seen with the disilicides. The observations of Souptel and Bulanova are paralleled with our observations with HoGaSi, showing the formation of the α-$GdSi_2$-type at higher temperature and the α-$ThSi_2$-type at lower temperature.

3.3. Lattice parameters of the Ga-flux grown crystals

Table 6 presents the refined compositions and lattice parameters for ten title compounds and for five previously known compounds in the *RE*GaSi series. For the latter, a comparison with a compound of similar refined composition, including *c*/*a* ratio is made. In all cases, the *c*/*a* ratios match well, with a slight difference in Sm compounds attributed to the different Ga:Si

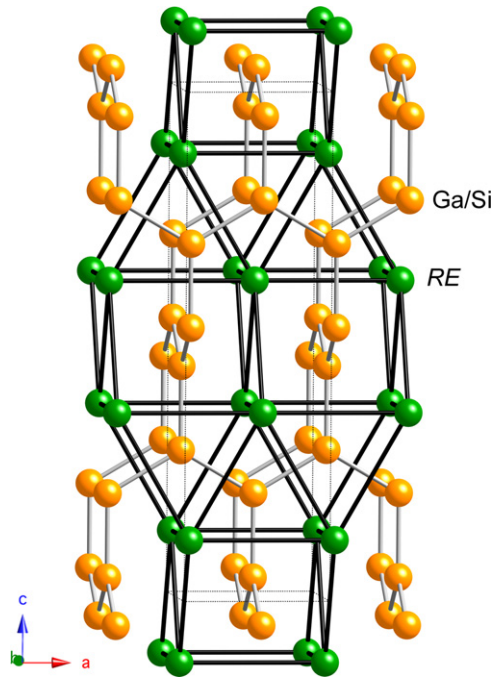

Fig. 1. The structure of the tetragonal $RE(Ga_{1-x}Si_x)_2$ (RE=La–Nd, Sm, Gd–Ho, Yb, Y; $0.37 \le x \le 0.63$) phases. Structure is isotypic with α-$ThSi_2$, the unit cell is outlined. RE positions shown in green, Ga/Si positions shown in orange. RE trigonal prism-based framework shown with black bonds. Ga/Si framework shown in gray bonds.

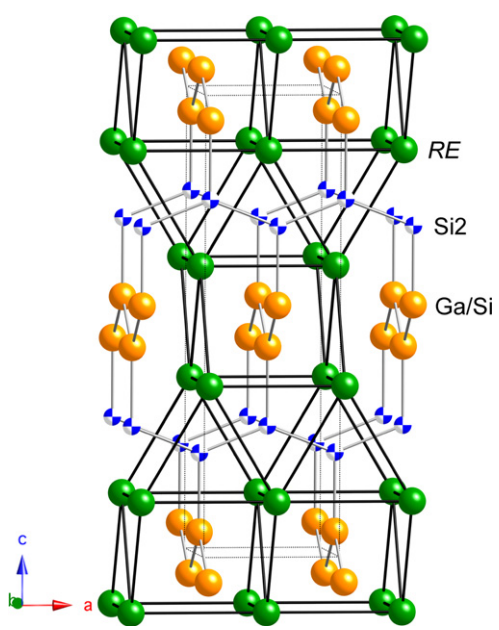

Fig. 2. The structure of the orthorhombic $REGa_xSi_{2-x-y}$ (RE=Ho, Er, Tm; $0.33 \le x \le 0.40$, $0.10 \le y \le 0.18$) phases. Structure is isotypic with α-$GdSi_2$, the unit cell is outlined. RE positions shown in green, Ga1/Si1 positions shown in orange, Si2 positions shown in blue/white checkers. The framework based on trigonal prisms of RE-atoms is shown with black bonds. Ga/Si framework shown in gray bonds.

ratio of the Ga-flux grown and stoichiometric arc-melted compounds. It should be noted that through control of the Ga:Si ratio available during synthesis in the Nd–Ga–Si system, via stoichiometric arc-melting, Tokaychuk et al. [14] were able to synthesize both α-$ThSi_2$-type crystals with empirical formulas ranging from $NdGa_{1.34}Si_{0.66}$ to $NdGa_{0.92}Si_{1.08}$ and α-$GdSi_2$-type crystals with empirical formulas ranging from $NdGa_{0.86}Si_{1.14}$ to $NdGa_{0.71}Si_{1.29}$.

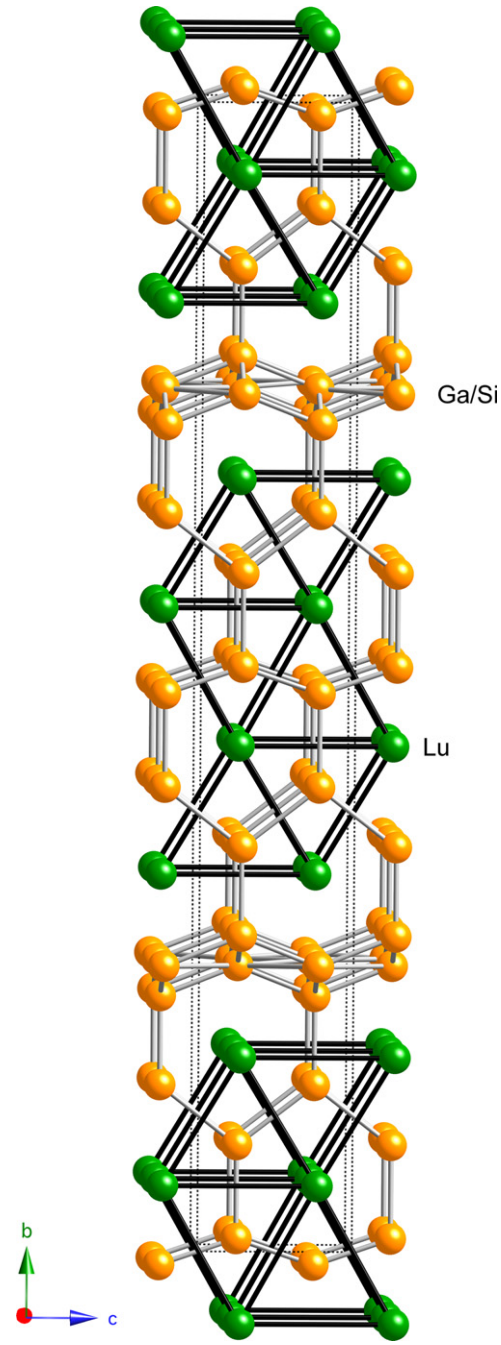

Fig. 3. The structure of the orthorhombic $LuGa_{0.32(1)}Si_{1.43(1)}$. Structure is isotypic with $YbMn_{0.17}Si_{1.83}$, the unit cell is outlined. The AlB_2-like framework of Lu atom positions is emphasized with black bonds, while the distorted Ga/Si network and the $BaAl_4$-like motifs are shown with gray bonds.

3.4. Effect of temperature on α-$ThSi_2$-type to α-$GdSi_2$-type transition in HoGaSi

Our initial Ga-flux synthesis of HoGaSi produced as the main phase, crystals which were characterized by single-crystal and powder X-ray diffraction as either α-$ThSi_2$-type (space group $I4_1/amd$) or α-$GdSi_2$-type (space group $Imma$). The crystals had the same physical appearance and could not be distinguished under an optical microscope, yet, the refinements show that their compositions are different. Papers by Perri et al. and Mayer et al. [45,46] discussed temperature-dependent polymorphism of the rare-earth disilicides, and so we suspected our inability to obtain

Table 6
Unit cell parameters (Å) for *RE*GaSi compounds.

Compound	Type	*a* (Å)	*b* (Å)	*c* (Å)	*V* (Å^3)	*c*/*a*	Reference
$LaGa_{0.84}Si_{1.16}$	α-$ThSi_2$	4.3087(16)		14.285(11)	265.2(2)	3.32	This paper
$LaGa_{0.77}Si_{1.23}$	α-$ThSi_2$	4.29(1)		14.23(1)	264.3(1)	3.32	[13]
$CeGa_{0.87}Si_{1.13}$	α-$ThSi_2$	4.2426(12)		14.274(8)	256.93(17)	3.36	This paper
$PrGa_{1.02}Si_{0.98}$	α-$ThSi_2$	4.2189(18)		14.296(12)	254.5(3)	3.39	This paper
$NdGa_{1.05}Si_{0.95}$	α-$ThSi_2$	4.1947(9)		14.290(6)	251.45(13)	3.41	This paper
$NdGa_{1.02}Si_{0.98}$	α-$ThSi_2$	4.1919(9)		14.249(6)	250.38(12)	3.40	This paper[a]
$NdGa_{1.04}Si_{0.96}$	α-$ThSi_2$	4.19308(4)		14.3105(2)	251.606(7)	3.41	[14]
$SmGa_{1.01}Si_{0.99}$	α-$ThSi_2$	4.1405(3)		14.209(2)	243.60(5)	3.43	This paper
$SmGa_{1.05}Si_{0.95}$	α-$ThSi_2$	4.1430(14)		14.202(10)	243.8(2)	3.43	This paper[a]
$SmGa_{1.10}Si_{0.90}$	α-$ThSi_2$	4.1479(1)		14.252(1)	245.2(1)	3.44	[13]
$GdGa_{1.23}Si_{0.77}$	α-$ThSi_2$	4.1298(9)		14.304(6)	243.96(12)	3.46	This paper
$GdGa_{1.16}Si_{0.84}$	α-$ThSi_2$	4.118(2)		14.242(13)	241.6(3)	3.45	This paper[a]
$TbGa_{1.18}Si_{0.82}$	α-$ThSi_2$	4.090(2)		14.222(14)	237.9(3)	3.48	This paper
$DyGa_{1.24}Si_{0.76}$	α-$ThSi_2$	4.0811(3)		14.231(2)	237.02(4)	3.49	This paper
$DyGa_{1.22}Si_{0.78}$	α-$ThSi_2$	4.08203(9)		14.2271(3)	237.07(2)	3.49	[15]
$HoGa_{1.12}Si_{0.88}$	α-$ThSi_2$	4.0658(9)		14.247(6)	235.51(12)	3.50	This paper
$YbGa_{0.76}Si_{1.24}$	α-$ThSi_2$	4.0957(5)		14.220(4)	238.53(7)	3.47	This paper
$YGa_{1.26}Si_{0.74}$	α-$ThSi_2$	4.0935(4)		14.255(3)	238.87(6)	3.48	This paper
$YGa_{1.27}Si_{0.73}$	α-$ThSi_2$	4.0939(9)		14.263(6)	239.04(13)	3.48	This paper[a]
$HoGa_{0.34}Si_{1.56}$	α-$GdSi_2$	3.970(2)	4.020(2)	13.401(7)	213.9(2)	3.38	This paper
$ErGa_{0.40}Si_{1.46}$	α-$GdSi_2$	3.9653(16)	4.0213(16)	13.424(5)	214.06(15)	3.39	This paper
$ErGa_{0.41}Si_{1.21}$	α-$GdSi_2$	3.9544(1)	4.0185(1)	13.3897(4)	212.78(1)	3.39	[16]
$TmGa_{0.33}Si_{1.50}$	α-$GdSi_2$	3.9283(18)	3.9961(18)	13.308(6)	208.90(16)	3.39	This paper
$LuGa_{0.32}Si_{1.43}$	$YbMn_{0.17}Si_{1.83}$	3.9678(10)	28.479(7)	3.8138(10)	430.95(19)	–	This paper

[a] Supporting information.

a single-phase material of this ternary compound might be the result of an equilibrium in which both crystal types compete at the given temperature regime. Hence, two different experiments were conducted, using identical stoichiometry as the original synthesis—the first experiment used a higher temperature (heated to 1573 K at 100 K/h, equilibration at this temperature for 24 h, cooled to 1073 K at 200 K/h, followed by an isotherm at this temperature for 35 h, after which the flux was removed and the grown-crystals isolated). The second experiment used the same ramp rate and reaction temperature, but the sample after 24 h equilibration at 1573 K was cooled to 773 K (again at 200 K/h), and annealed at this temperature for 35 h. The higher temperature route produced α-$GdSi_2$-type crystals, with refined empirical formula of $HoGa_{0.34(3)}Si_{1.56(5)}$, and with lattice parameters of a=3.970(2) Å, b=4.020(2) Å, c=13.401(7) Å, V=213.9(2) Å^3. The lower temperature route produced α-$ThSi_2$-type crystals (a very small amount of the α-$GdSi_2$-type was also present according to the powder X-ray diffractograms, suggesting the isolation of the two phases was not complete), with refined empirical formula of $HoGa_{1.12}Si_{0.88(4)}$, and with lattice parameters of a=4.0658(9) Å, c=14.247(6) Å, V=235.51(12) Å^3. Then, a follow-up experiment was conducted with the already-grown α-$GdSi_2$-type crystals—they were reheated to 873 K in an evacuated quartz tube with an excess of Ga, and annealed at this temperature for 250 h. This treatment resulted in a partial transformation of the crystals from α-$GdSi_2$-type to α-$ThSi_2$-type, and the formation of small Si crystals on the exterior, a result of the escape of Si from the crystal structure in the transformation from Si-rich α-$GdSi_2$-type to Ga-rich α-$ThSi_2$-type. Diffractograms for the high-temperature, low-temperature, and annealed crystals are shown in Fig. 4. As mentioned previously, these findings mirror the findings of Bulanova et al. for the binary rare-earth disilicides.

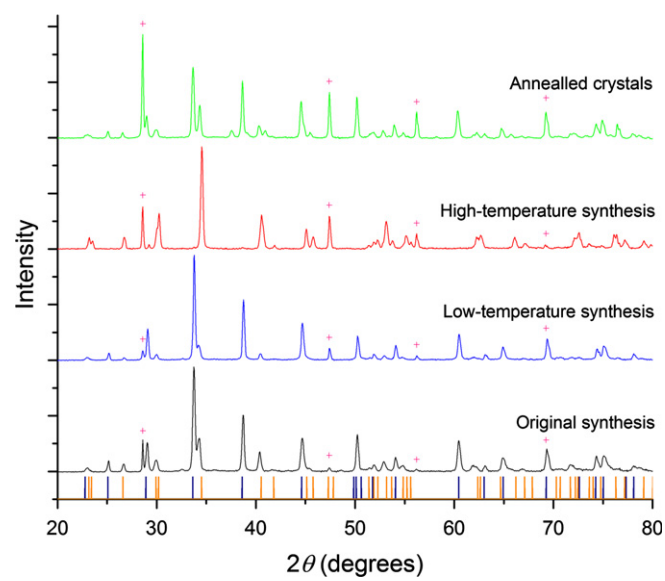

Fig. 4. Powder X-ray diffraction patterns for the products of the original synthesis of HoGaSi (black line), low-temperature synthesis of tetragonal α-$ThSi_2$-type HoGaSi (blue line), high-temperature synthesis of orthorhombic α-$GdSi_2$-type HoGaSi (red line), annealed orthorhombic HoGaSi (green line). Peaks corresponding to elemental Si are denoted cross-marks. Simulated peaks from refined parameters for α-$ThSi_2$-type HoGaSi shown at bottom in purple, and for α-$GdSi_2$-type HoGaSi shown in orange (For interpretation of the references to color in this figure legend, the reader is referred to the web version of this article.).

3.5. Magnetic susceptibility

Temperature-dependent DC magnetization measurements were performed on polycrystalline samples of the *RE*GaSi (*RE*=Ce–Nd, Sm, Gd–Yb) compounds. Field and zero-field cooled data were gathered in the temperature range 2–300 K, under applied fields of 10, 500 or 5000 Oe. The data were converted to molar magnetic susceptibility ($\chi_m = M/H$), and $\chi_m(T)$ plots are shown in Figs. 5–10. In the high-temperature regime, all samples are paramagnetic as expected for compounds with core 4*f* electrons. YbGaSi shows typical Pauli-like paramagnetic behavior, indicating Yb^{2+} state ([Xe]4f^{14}). The data for *RE*GaSi (*RE*=Ce–Nd, Gd–Tm) follow the Curie–Weiss law, $\chi(T) = C/(T-\theta_p)$, where C is the Curie constant ($N_A\mu_{eff}^2/3k_bT$), and θ_p is the paramagnetic Weiss temperature [47]. Curie constants and correspondingly, the effective paramagnetic moments (p_{eff}) and θ_p of these compounds can

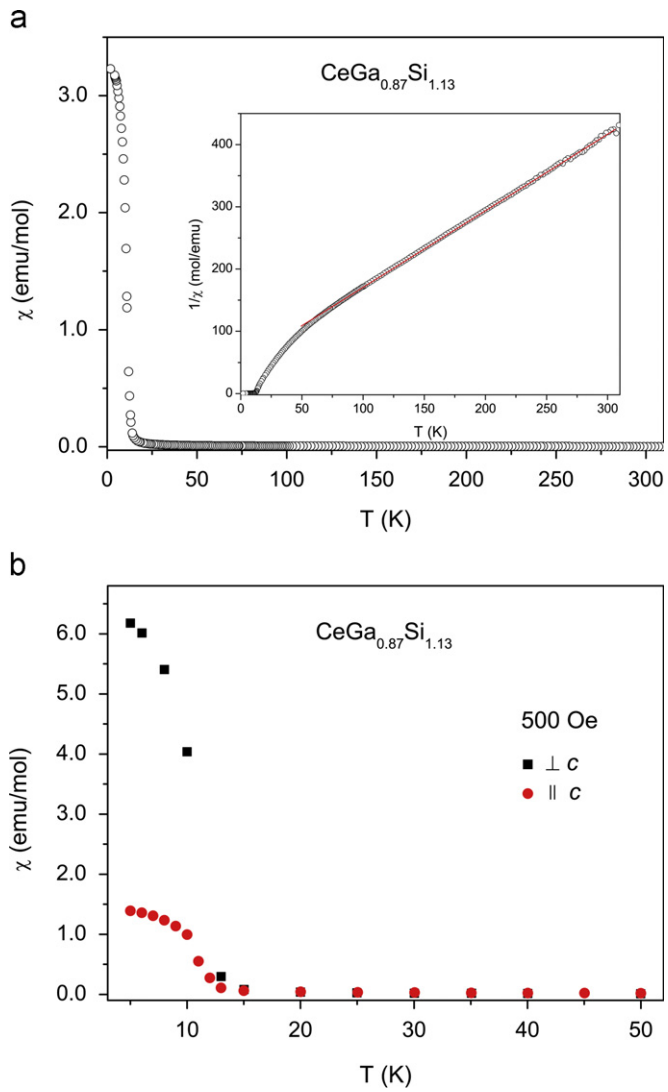

Fig. 5. (a) Molar magnetic susceptibility of $CeGa_{0.87}Si_{1.13(1)}$ vs temperature; data measured under an applied field of 1000 Oe. The inset shows the inverse molar susceptibility and a linear fit to the Curie–Weiss law. (b) Magnetization under an applied filed of 500 Oe in directions perpendicular and parallel to the *c* axis.

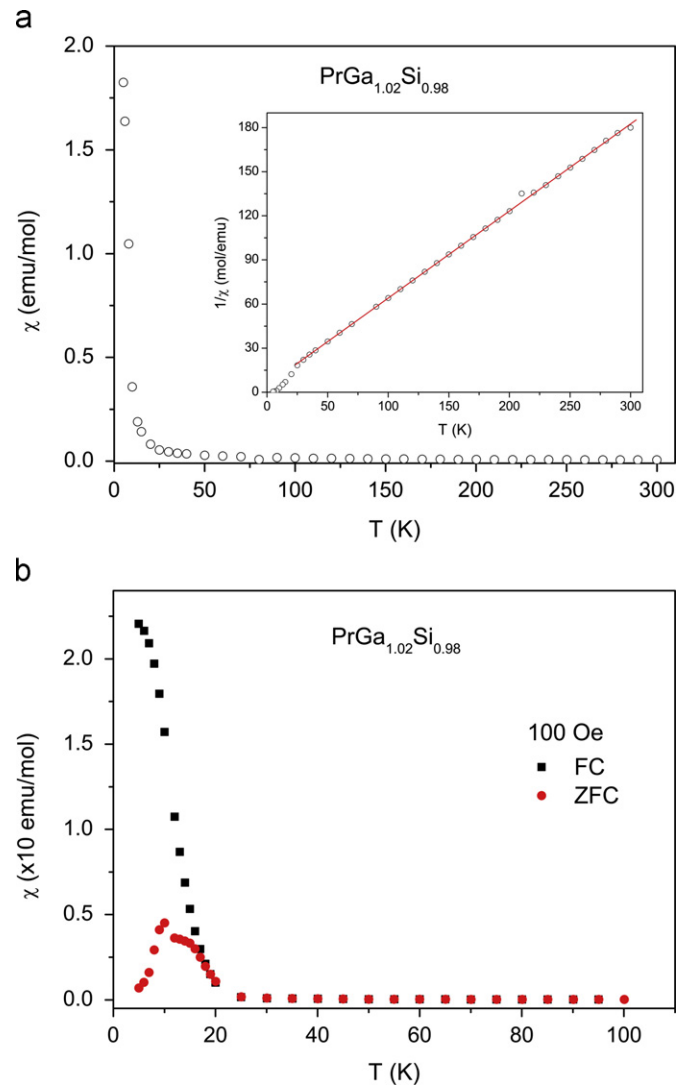

Fig. 6. (a) Molar magnetic susceptibility of $PrGa_{1.02}Si_{0.98(4)}$ vs temperature; data measured under an applied field of 1000 Oe. The inset shows the inverse molar susceptibility and a linear fit to the Curie–Weiss law. (b) The FC and ZFC magnetization along the basal plane.

be calculated from linear regression of the $1/\chi_m(T)$ plots, and are summarized in Table 7. $SmGa_{1.01}Si_{0.99}$ shows the characteristic Van Vleck-type paramagnetism, where the significant contribution of the temperature-independent term, χ_o, to the total molar susceptibility is accounted for with the modified Curie–Weiss law, $\chi_m(T)=\chi_o+C/(T-\theta_p)$ [47]. The effective moment and θ_p in this instance were obtained from a non-linear fit to $\chi_m(T)$ and are also listed in Table 7. All observed moments are consistent with the values expected for free-ion RE^{3+} species according to the Hund's rule [47].

In the low-temperature regime, the magnetization curves for most of the measured samples show the onsets of magnetic ordering, as seen from the $\chi_m(T)$ plots in Figs. 5–10. The magnetic behaviors seem complicated and dependent on the nature of the rare-earth elements, as well as the structure and will be discussed on a case-to-case basis.

3.6. CeGaSi

The temperature-dependent magnetization of the CeGaSi compound was measured under an applied field of 1000 Oe. As shown in Fig. 5, the unfinished transition cannot reveal the nature of ordering directly, but the high susceptibility suggests a ferromagnetic ordering at low temperatures. The ferromagnetic ordering is more evident from the inset plot of $1/\chi_m(T)$. Previous studies on $CeGa_xSi_{2-x}$ ($x=0.7$, 1.0, 1.3) have shown the domination of ferromagnetic exchange interactions in the ranges and the increased Ga concentration depressed the ordering temperature from 12 K to 2 K [48]. The present compound with $x=0.87(1)$ has an ordering temperature of ca. 10 K, in agreement with the earlier reported results. Neutron scattering experiments [49] combined with physical measurements [50] have revealed that $CeGa_xSi_{2-x}$ ($x=1.0$, 1.3) belong to the magnetic concentrated Kondo systems (CKS), while for $x=0.7$, the material is magnetic 4*f*-metal (but close to the boundary of the CKS). Thus, the studied single-crystalline $CeGa_{0.87}Si_{1.13(1)}$ compound should be a ferromagnetic concentrated Kondo system, characterized by two Kondo temperatures. The effective moment and θ_p obtained from the fitting of Curie–Weiss rule are 2.55 μ_B and −40.5 K respectively. Such negative θ_p generally indicates antiferromagnetic exchange interactions, similar to those in some other ferromagnetic Ce-based silicides with negative θ_p, such as $CeAl_{1.2}Si_{0.8}$ [51] and $CeGa_{1.4}Si_{0.6}$ [52].

We can attribute such antiferromagnetic correlations existing in these ferromagnets to the transition from ferromagnetic to

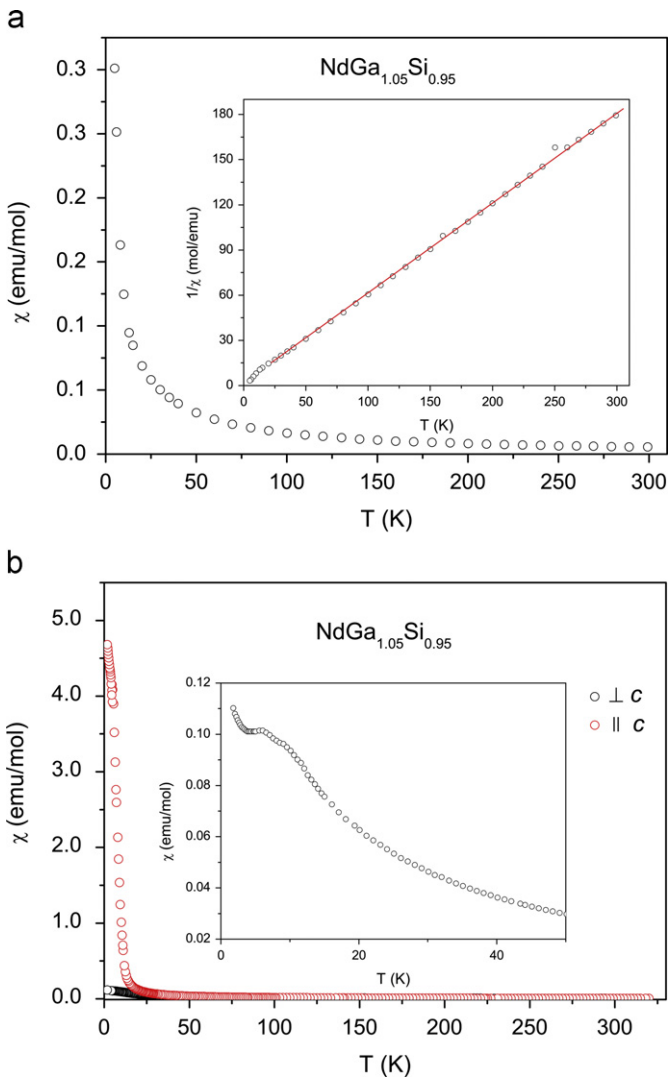

Fig. 7. Temperature dependence of the molar magnetic susceptibility of NdGaSi in polycrystalline (a) and single-crystalline form (b). Both data are gathered under an applied filed of 1000 Oe. The inset in (a) shows the inverse molar susceptibility and linear fits to the Curie–Weiss law. The inset in (b) presents the close view of ordering transitions in the basal plane.

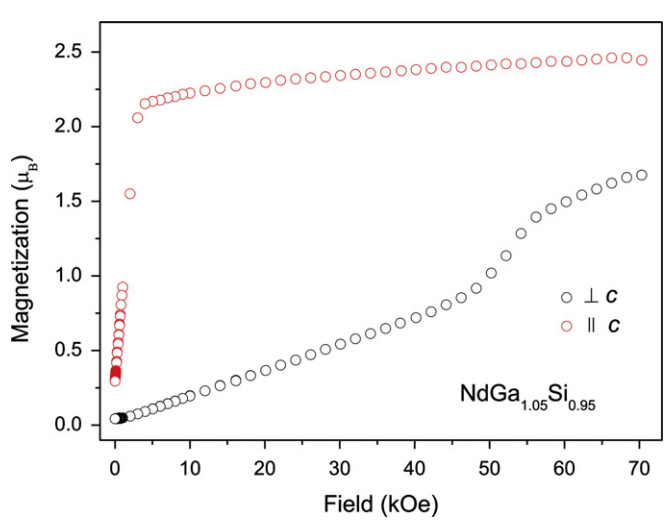

Fig. 8. Field dependence of magnetizations for the NdGaSi single crystals along and perpendicular to the *c*-axis.

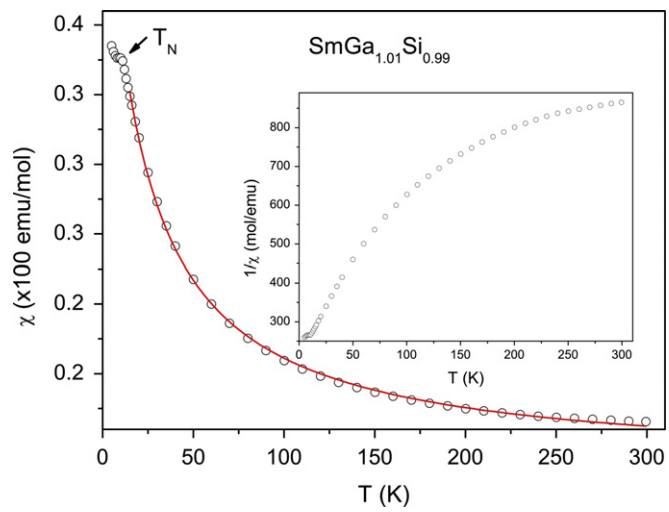

Fig. 9. Molar magnetic susceptibility of $SmGa_{1.01}Si_{0.99(1)}$ vs temperature; data measured under an applied field of 1000 Oe. The solid red line represents the non-linear fit to the modified Curie–Weiss law; the inset shows the inverse molar susceptibility.

non-magnetic and then to antiferromagnetic states [52]. After all, almost all other *RE*GaSi are antiferromagnets. This supposition is based on prior neutron diffraction experiments [53] and magnetization measurements [54], which have shown that in binary rare-earth metal silicides with the α-$ThSi_2$ and α-$GdSi_2$-type structures, the ferromagnetic interactions are confined in the basal planes and the interplane interactions are often antiferromagnetic. We also conducted temperature-dependent magnetization on oriented single-crystal CeGaSi. As shown in Fig. 5(b), the sample is easily magnetized in the basal plane; the ordering temperature likely originates from the long-axis magnetization. It should be noted that the magnetization along the *c*-axis exhibit behavior similar to ferromagnets instead of antiferromagnets, favoring a pronounced magnetocrystalline anisotropy, and not antiferromagnetic interactions. However, the strong deviation of the $1/\chi_m(T)$ plot from the linearity below 100 K together with a negative value is a good indication for a 'ferrimagnetic-like' ground state, as occurred in CeSb or CeBi compounds [55,56]. More experiments especially neutron diffractions are called to precisely determine the magnetic exchange interaction in the compound.

3.7. PrGaSi

The temperature-dependent magnetization under an applied field of 1000 Oe is shown in Fig. 6(a). Fitting of $1/\chi_m(T)$ with the Curie–Weiss law yields an effective moment of 3.60 μ_B and θ_p of −8.6 K. The negative θ_p value again suggests an antiferromagnetic interaction, but the low-temperature susceptibility of PrGaSi is much larger than that of other antiferromagnetic *RE* counterparts. To determine the magnetic nature of the compound, field cooling (FC) and zero-field cooling (ZFC) magnetization were performed on single-crystal samples along the basal plane, as shown in Fig. 6(b). It should be also noted here that the measurements were conducted in the same direction with very weak applied field (100 Oe). The FC magnetization data appear to support the notion for ferromagnetic interactions (FC curve continuously rises with decreasing temperature), whilst the ZFC magnetization is reminiscent with antiferromagnetic-like behavior (the ZFC curve peaks just below T_C, followed by a drastic fall in the magnetization value).

Based on the above, we propose that the magnetic ordering in PrGaSi is ferromagnetic type with Curie temperature below 10 K.

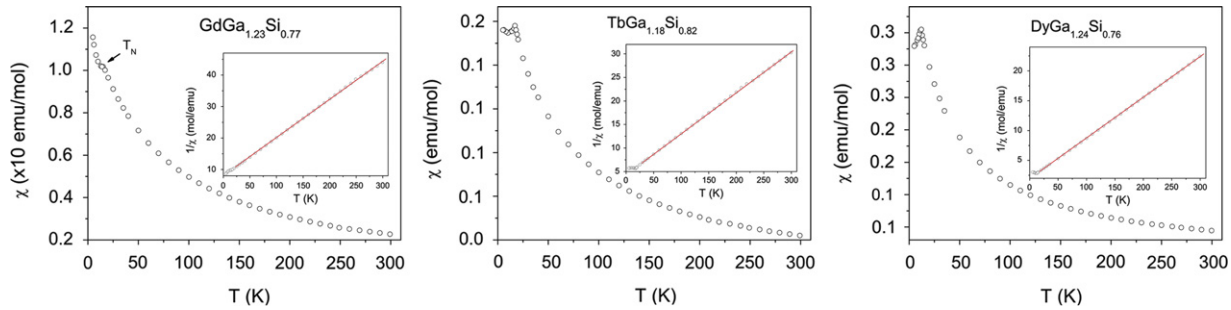

Fig. 10. Temperature dependence of the molar magnetic susceptibility of *RE*GaSi (*RE*=Gd, Tb, Dy) compounds, all with the tetragonal α-$ThSi_2$-type structure. Data obtained under an applied field of 1000 Oe. The insets show their inverse molar susceptibilities and linear fits to the Curie–Weiss law.

Table 7
Selected magnetic data for the *RE*GaSi compounds.

Compounds	Structure	Ordering	T_N/T_C (K)	θ_p (K)	p_{eff} (μ_B)
$CeGa_{0.87}Si_{1.13}$	α-$ThSi_2$	FM-like	10	−40.5	2.55
$PrGa_{1.02}Si_{0.98}$	α-$ThSi_2$	FM-like	17	−8.6	3.60
$NdGa_{1.05}Si_{0.95}$[a]	α-$ThSi_2$	AFM	<5	−0.9	3.64
$NdGa_{1.05}Si_{0.95}$[b]	α-$ThSi_2$	AFM	5	−2.7	3.52
$NdGa_{1.05}Si_{0.95}$[c]	α-$ThSi_2$	FM	10	8.9	3.60
$SmGa_{1.01}Si_{0.99}$	α-$ThSi_2$	AFM	10	−18.3	0.85
$SmGa_{1.05}Si_{0.95}$	α-$ThSi_2$	AFM	10	−14.9	0.84
$GdGa_{1.23}Si_{0.77}$	α-$ThSi_2$	AFM	15	−63	8.06
$TbGa_{1.18}Si_{0.82}$	α-$ThSi_2$	AFM	17	−49.2	9.55
$DyGa_{1.24}Si_{0.76}$	α-$ThSi_2$	AFM	12	−27.2	10.80
$HoGa_{1.12}Si_{0.74}$	α-$ThSi_2$	AFM	<5	−9	10.54
$HoGa_{0.34}Si_{1.56}$	α-$GdSi_2$	AFM	11	−11.8	10.62
$ErGa_{0.40}Si_{1.88}$	α-$GdSi_2$	AFM	9	3.0	9.63
$TmGa_{0.33}Si_{1.50}$	α-$GdSi_2$	AFM	4	6.5	7.60

[a] Polycrystalline sample.
[b] Single-crystal || *ab*.
[c] Single-crystal || *c*.

The peak in the ZFC data and the decrease in $\chi_m(T)$ below ca. 10 K is likely not characteristic of a long-range ordered FM systems in which the magnetization below T_C varies as the inverse of the demagnetization factor and is expected to be constant. However, in the case of FM systems, we can see a bifurcation of ZFC–FC curves if the coercive field becomes larger than the externally applied field. Similar observations have been reported for the PrAlSi compound [22], as well as for the $PrSi_{1.88}$ [57] and CeSi [58] phases. Clearly, to fully understand the nature of the magnetism here, additional AC-type magnetization measurements are required.

3.8. NdGaSi

Polycrystalline NdGaSi exhibits classic antiferromagnetic behavior, as shown in Fig. 7(a). The Curie–Weiss fit shows θ_p close to 0 K in NdGaSi, which is suggestive of a balance between the ferromagnetic and the antiferromagnetic interactions in this compound. It also supports the idea that the ferromagnetic interactions are dominant in earlier *RE* analogs and the antiferromagnetic interactions prevail for the later *RE* compounds. The trend is similar to that in $RESi_{2-x}$ [59]. Considering the large magnetic anisotropy known for many Nd-based compounds, NdGaSi can also be expected to show anisotropic behavior, which is confirmed from the plots in Fig. 7(b). It is evident that the magnetic interactions are ferromagnetic in nature with a Curie temperature of ca. 10 K, when the measurements are taken along the *c*-axis; on the other hand, clear indication of antiferromagnetic ordering with a Neel temperature of ca. 5 K are seen when the measurements are taken in the basal plane. The Curie–Weiss fit shows close p_{eff} in both directions, but the paramagnetic Curie temperatures are significantly different even in sign: θ_p=8.9 K along *c*-axis and θ_p=−2.7 K in the basal plane, as seen in Table 7 and Fig. S2. These results are in good agreement with the two kinds of magnetic interactions and results of polycrystalline samples. The inset in Fig. 7(b) shows that there are multiple transitions in the compound, and thus, the cusp of antiferromagnetic transition is depressed. One may argue that the small susceptibility in the basal plane results from the crystal-field effects. The measured field dependent magnetization at 1.8 K, presented in Fig. 8, supports the notion of strong ferromagnetic interactions along the *c*-axis. The magnetic moment at 3000 Oe is already close to its saturation of ~2.5 μ_B. The saturation is comparable with, or even larger than, that in other ferromagnetic Nd compounds [60]. In the basal plane direction, the linear dependence on the applied field up to 50 kOe is in excellent agreement with the proposed antiferromagnetic behavior. Similar effects of anisotropy have been discussed above for the CeGaSi compound, but there are two significant differences between two cases: (1) the susceptibility along the hard-magnetization axis is more than ten times larger in CeGaSi; (2) the hard-magnetization direction is along the *c*-axis in CeGaSi, but in the basal plane in NdGaSi, despite their similar structure. The idea of strong magnetocrystalline anisotropy of the ferromagnetic interactions in CeGaSi agrees well with data, while the competition between the ferromagnetic and antiferromagnetic interactions in NdGaSi can be cited as the reason for the behavior in this material. Also, as seen in Table 1, NdGaSi has a smaller *a*-axis, but larger *c*-axis compared with CeGaSi, which could be explained by the small compositional difference, although from available structural data for $Nd(Ga_{1-x}Si_x)_2$ ($0.33<x<0.54$) [14], one might conclude that even for the same Ga:Si ratio, the Nd-sample will have larger *c*-axis than its Ce-counterpart. This likely is due to the enhanced Nd–Nd interactions in the basal plane, leading to the strong antiferromagnetic interactions in the NdGaSi.

3.9. SmGaSi

This compound is an antiferromagnet at cryogenic temperatures, as seen from the cusp of the $\chi_m(T)$ data around 10 K (Fig. 9). The Sm^{3+} moments could undergo successive magnetic ordering(s) at even lower temperature, and more work is needed to characterize this material. Such a hypothesis is based on our previous investigation on Sm-based germanides, which has shown that secondary transitions are typically concealed by the applied field [61].

3.10. GdGaSi, TbGaSi, and DyGaSi

All three compounds are classical antiferromagnets, as characterized by the small and converged susceptibility (Fig. 10). The data clearly show transition temperatures of 15 K for GdGaSi,

17 K for TbGaSi, and 12 K for DyGaSi, suggestive of non-DeGennes scaling.

3.11. HoGaSi

Recall that there are two compounds with slightly different composition and structures here. The magnetization curves for both are shown in Fig. 11. The data indicate that $HoGa_{0.34(3)}Si_{1.56(5)}$ (α-$GdSi_2$ type) has a much higher ordering temperature than that of $HoGa_{1.12}Si_{0.88(4)}$ (α-$ThSi_2$ type), albeit both enter into antiferromagnetic ground state. Detailed studies on $CeSi_{2-x}$ ($1.6 < x < 1.9$) have shown that small structural variations accompanied by small composition changes affect the ordering temperature by less than 1 K [62]. On the other hand, increase in the Si-vacancies elevates the ordering temperature effectively due to the enhanced exchange interactions characterized by the shorter Ce–Ce contacts in structures with a greater number of defects [62]. In the case of HoGaSi, Ho–Ho interactions are reduced by increased Ga content and by the lack of structural defects on the Ga/Si site in the α-$ThSi_2$ type material. For instance, the shortest Ho–Ho distance is 4.0658(9) Å in $HoGa_{1.12}Si_{0.88(4)}$, while shorter Ho–Ho distances of 3.8965 Å and 3.9047 Å are refined for $HoGa_{0.34(3)}Si_{1.56(5)}$. Extrapolating from our previous work on the *RE*–Al–Si systems [22], one can expect that the *RE*AlSi compounds will have higher ordering temperatures compared to their *RE*GaSi counterparts with the same α-$ThSi_2$ structure. Indeed, $GdAl_{0.92}Si_{1.02}$ shows higher T_N (32 K) than $GdGa_{1.23}Si_{0.77}$ (15 K) in agreement with the Gd–Gd contacts—4.1255(1) Å and 4.1294(9) Å, respectively. On the other hand, $SmAl_{1.07}Si_{0.93}$ shows slightly lower ordering T_N (9 K) than $SmGa_{1.01}Si_{0.99}$ (10 K) because of the reverse trend in the Sm–Sm distances—4.1577(1) Å and 4.1405(3) Å, respectively. It seems that the *RE*–*RE* distances affect exchange interactions more significantly *RE*-compounds with collinear *RE* sub-lattices, owing to the small magnetocrystalline anisotropy.

3.12. ErGaSi and TmGaSi

The magnetization plots shown in Fig. 12 indicate the antiferromagnetic nature of both compounds. The ordering temperatures are 10 K for ErGaSi and 4 K for TmGaSi respectively. Unlike other compounds in the study, both compounds show a positive θ_p despite their antiferromagnetic nature. It is also the case of some other Er-based or Tm-based compounds [63], which was generally attributed to the large crystalline anisotropy of the later

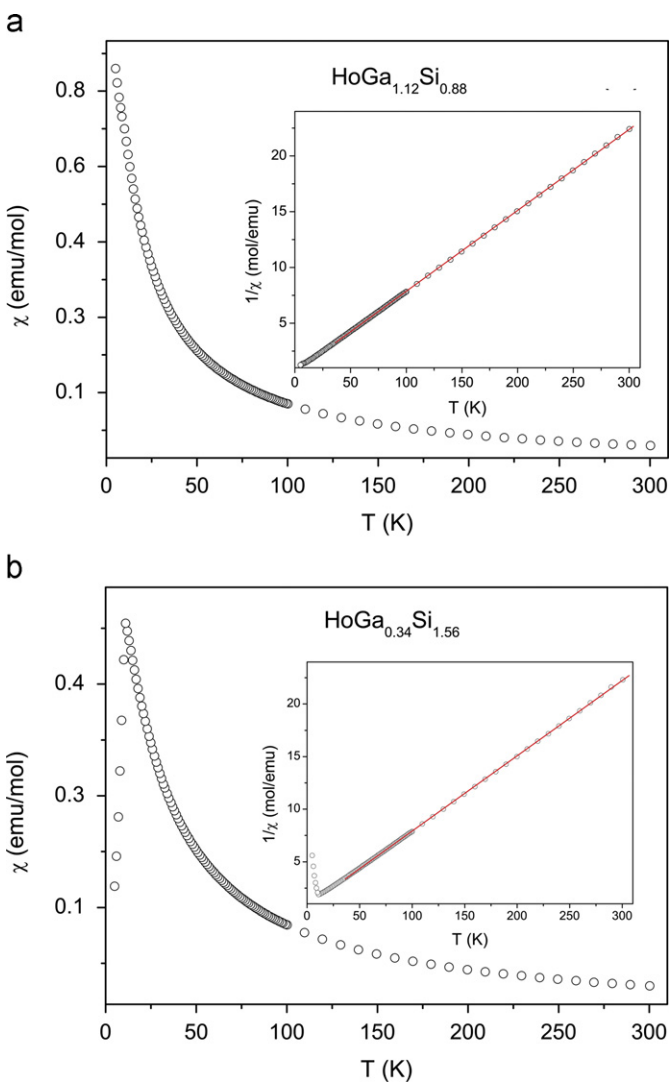

Fig. 11. (a) Molar magnetic susceptibility vs temperature of $HoGa_{1.12}Si_{0.88(4)}$ (α-$ThSi_2$ structure type). (b) Molar magnetic susceptibility vs temperature of $HoGa_{0.34(3)}Si_{1.56(5)}$ (α-$GdSi_2$ structure type). Data were obtained under an applied field of 1000 Oe. The insets show their inverse molar susceptibilities and linear fits to the Curie–Weiss law.

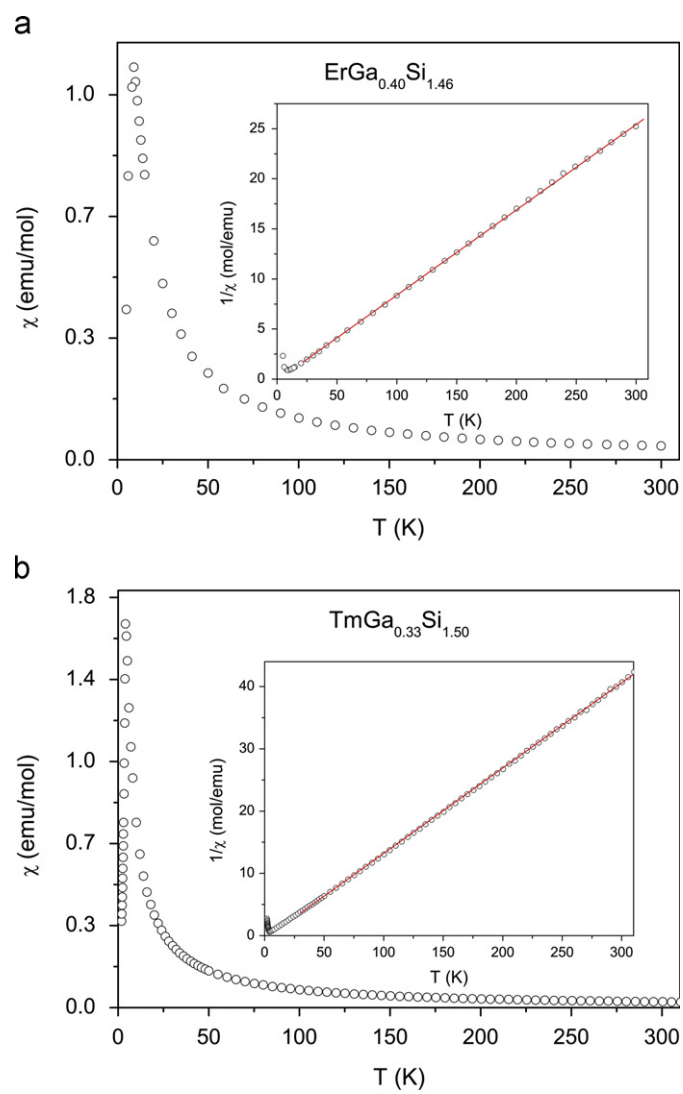

Fig. 12. Molar magnetic susceptibility of $ErGa_{0.40(2)}Si_{1.46(4)}$ (a) and $TmGa_{0.33(2)}Si_{1.50(4)}$ (b) vs temperature. Data were obtained under an applied field of 1000 Oe. The insets show their inverse molar susceptibilities and linear fits to the Curie–Weiss law.

RE metals. The enhanced crystalline anisotropy is manifest from the lattice constants of ErGaSi, with a smaller *a*, but larger *b* and *c* compared with the HoGaSi compound.

Acknowledgments

Svilen Bobev acknowledges financial support from the National Science Foundation through a grant DMR-0743916 (CAREER). Work at the University of Maryland was supported by AFOSR-Multidisciplinary University Research Initiative Grant No. FA9550-09-1-0603.

Appendix A. Supporting information

Supplementary data associated with this article can be found in the online version at http://dx.doi.org/10.1016/j.jssc.2013.02.029. The information consists of tables with crystallographic information for $RE(Ga_{1-x}Si_x)_2$ (RE=Nd, Sm, Gd, Ho, Y) and $TmGa_xSi_{2-x-y}$, grown from more dilute Ga solutions, representative powder diffraction patterns, a plot with the temperature dependence of the inverse molar magnetic susceptibility of NdGaSi singlecrystals along and perpendicular to the c-axis.

References

[1] (a) G.F. Hardy, J.K. Hulm, Phys. Rev. 93 (1954) 1004–1016;
(b) E. Zurek, O. Jepsen, O.K. Andersen, Inorg. Chem. 49 (2010) 1384–1396.
[2] J. Nagamatsu, N. Nakagawa, T. Muranaka, Y. Zenitani, J. Akimitsu, Nature 410 (2001) 63–64.
[3] M. Imai, E. Abe, J. Ye, K. Nishida, T. Kimura, K. Honma, H. Abe, H. Kitazawa, Phys. Rev. Lett. 87 (2001) 077003-1-077003-4.
[4] M. Imai, K. Nishida, T. Kimura, H. Abe, Phys. C 377 (2002) 96–100.
[5] M. Imai, K. Nishida, T. Kimura, H. Kitazawa, H. Abe, H. Kito, K. Yoshii, Phys. C 382 (2002) 361–366.
[6] M. Imai, K. Nishida, T. Kimura, H. Abe, Appl. Phys. Lett. 80 (2002) 1019–1021.
[7] B. Lorenz, J. Lenzi, J. Cmaidalka, R.L. Meng, Y.Y. Sun, Y.Y. Xue, C.W. Chu, Phys. C 383 (2002) 191–196.
[8] B. Lorenz, J. Cmaidalka, R.L. Meng, C.W. Chu, Phys. Rev. B 68 (2003) 014512-1-014512-6.
[9] I.R. Shein, N.I. Medvedeva, A.L. Ivanovskii, J. Phys.: Condens. Matter 15 (2003) L541–L545.
[10] H.H. Sung, W.H. Lee, Phys. C 406 (2004) 15–19.
[11] A. Raman, H. Steinfink, Inorg. Chem. 6 (1967) 1789–1791.
[12] M. Imai, T. Aoyagi, T. Kimura, Intermetallics 16 (2008) 96–101.
[13] Ya.O. Tokajchuk, A.A. Fedorchuk, I.R. Mokra, Pol. J. Chem. 74 (2000) 745–748.
[14] Ya.O. Tokaychuk, A.O. Fedorchuk, O.I. Bodak, I.R. Mokra, J. Alloys Compd. 367 (2004) 64–69.
[15] O. Bodak, J. Tokaychuk, A. Fedorchuk, I. Mokra, Visn. Lviv. Univ. Ser. Khim. 44 (2004) 41–43.
[16] S.Ya. Pukas, R. Cherni, M.B. Manyako, R.E. Hlad, Ukr. Khim. Zh. 73 (2007) 18–26.
[17] T.S. You, Y. Grin, G.J. Miller, Inorg. Chem. 46 (2007) 8801–8811.
[18] M. Imai, A. Sato, T. Aoyagi, T. Kimura, Y. Matsushita, N. Tsujii, J. Am. Chem. Soc. 130 (2008) 2886–2887.
[19] T.S. You, J.T. Zhao, R. Pöttgen, W. Schnelle, U. Burkhardt, Y. Grin, G.J. Miller, J. Solid State Chem. 182 (2009) 2430–2442.
[20] I. Yoznyak, Ya. Tokaychuk, V. Hlukhyy, T. Fässler, R. Gladyshevskii, Visn. Lviv. Univ. Ser. Khim. 52 (2011) 78–83.
[21] S. Bobev, V. Fritsch, J.D. Thompson, J.L. Sarrao, B. Eck, R. Dronskowski, S.M. Kauzlarich, J. Solid State Chem. 178 (2005) 1071–1079.
[22] S. Bobev, P.H. Tobash, V. Fritsch, J.D. Thompson, M.F. Hundley, J.L. Sarrao, Z. Fisk, J. Solid State Chem. 178 (2005) 2091–2103.
[23] S. Bobev, V. Fritsch, J.D. Thompson, J.L. Sarrao, J. Solid State Chem. 179 (2006) 1035–1040.
[24] P.H. Tobash, S. Bobev, J. Alloys Compd. 418 (2006) 58–62.
[25] S.Q. Xia, J. Hullmann, S. Bobev, J. Solid State Chem. 181 (2008) 1909–1914.
[26] H. He, R. Stearrett, E.R. Nowak, S. Bobev, Inorg. Chem. 49 (2010) 7935–7940.
[27] S. Bobev, E.D. Bauer, J.D. Thompson, J.L. Sarrao, J. Magn. Magn. Mater. 277 (2004) 236–243.
[28] SMART NT, Version 5.63; Bruker Analytical X-ray Systems Inc., Madison, WI, U.S.A., 2003.
[29] SAINT NT, Version 6.45; Bruker Analytical X-ray Systems Inc., Madison, WI, U.S.A., 2003.
[30] SADABS NT, Version 2.10; Bruker Analytical X-ray Systems Inc., Madison, WI, U.S.A., 2001.
[31] SHELXTL, Version 6.12; Bruker Analytical X-ray Systems Inc.; Madison, WI, U.S.A., 2001.
[32] L.M. Gelato, E. Parthé, J. Appl. Crystallogr. 20 (1987) 139–146.
[33] L. Pauling, The Nature of the Chemical Bond, third ed., Cornell University Press, Ithaca, 1960, p. 403.
[34] N.M. Norlidah, I. Ijjaali, G. Venturini, B. Malaman, J. Alloys Compd. 278 (1998) 246–251.
[35] M.J. Evans, Y. Wu, V.F. Kranak, N. Newman, A. Reller, F.J. Garcia-Garcia, U. Häussermann, Phys. Rev. B 80 (2009) 064514-1-064514-11.
[36] H. Wang, S. Misra, F. Wang, G.J. Miller, Inorg. Chem. 49 (2010) 4586–4593.
[37] P. Demchenko, O. Bodak, L. Muratova, J. Alloys Compd. 346 (2002) 170–175.
[38] Y. Murashita, J. Sakurai, T. Satoh, Solid State Commun. 77 (1991) 789–792.
[39] E. Houssay, A. Rouault, O. Thomas, R. Madar, J.P. Senateur, Appl. Surf. Sci. 38 (1989) 156–161.
[40] D. Souptel, G. Behr, W. Löser, A. Teresiak, S. Drotziger, C. Pfleiderer, J. Cryst. Growth 269 (2004) 606–616.
[41] M.V. Bulanova, P.N. Zheltov, K.A. Meleshevich, P.A. Saltykov, G. Effenberg, J.-C. Tedenac, J. Alloys Compd. 329 (2001) 214–223.
[42] M.V. Bulanova, P.N. Zheltov, K.A. Meleshevich, P.A. Saltykov, G. Effenberg, J. Alloys Compd. 345 (2002) 110–115.
[43] B. Lambert-Andron, N. Boutarek, J. Pierre, R. Madar, J. Alloys Compd. 203 (1994) 1–6.
[44] A.M. Guloy, J.D. Corbett, Inorg. Chem. 30 (1991) 4789–4794.
[45] J.A. Perri, E. Banks, B. Post, J. Phys. Chem. 63 (1959) 2073–2074.
[46] I. Mayer, E. Yanir, I. Shidlovsky, Inorg. Chem. 6 (1967) 842–844.
[47] J.S. Smart, Effective Field Theories of Magnetism, Saunders, Philadelphia, 1966.
[48] [a] H. Mori, N. Sato, T. Satoh, Solid State Commun. 49 (1984) 955;
[b] V.V. Moshchalkov, O.V. Petrenko, M.K. Zalyalutdinov, Phys. B 163 (1990).
[49] K.R. Priolkar, M.N. Rao, R.B. Prabhu, P.R. Sarode, S.K. Paranjpe, P. Raj, A. Sathyamoorthy, J. Magn. Magn. Mater. 185 (1998) 375.
[50] K.R. Priolkar, R.B. Prabhu, P.R. Sarode, V. Ganesan, P. Raj, A. Sathyamoorthy, J. Phys.: Condens. Matter 10 (1998) 4413.
[51] S.K. Dhar, S.M. Pattalwar, J. Magn. Magn. Mater. 152 (1996) 22.
[52] K.R. Priolkar, S.M. Pattalwar, P.K. Mishra, P. Raj, A. Sathyamoorthy, S.K. Dhar, V.C. Sahni, P.R. Sarode, R.B. Prabhu, Solid State Commun. 104 (1997) 71.
[53] N. Sato, M. Kohgi, T. Satoh, Y. Ishikawa, H. Hiroyoshi, H. Takei, J. Magn. Magn. Mater. 52 (1985) 360.
[54] J. Pierre, S. Auffret, E. Siaud, R. Madar, E. Houssay, A. Rouault, J.P. Senateur, J. Magn. Magn. Mater. 89 (1990) 86.
[55] J. Rossat-Mignod, P. Burlet, J. Villain, H. Bartholin, W. Tcheng-Si, D. Florence, O. Vogt, Phys. Rev. B 1 (1977) 440.
[56] H. Bartholin, P. Burlet, S. Quezel, J. Mignod, O. Vogt, J. Phys. 40 (1979) C5130.
[57] N. Pinguet, F. Weitzer, K. Hiebl, J.C. Schuster, H. Noël, J. Alloys Compd. 348 (2003) 1.
[58] S.A. Shaheen, W.A. Mendoza, Phys. Rev. B 60 (1999) 9501.
[59] K. Sekizawa, K. Yasukochi, J. Phys. Soc. Jpn. 21 (1966) 274.
[60] J. Zhang, P.H. Tobash, W.D. Pryz, D.J. Buttey, N. Hur, J.D. Thompson, J.L. Sarrao, S. Bobev, Inorg. Chem. 52 (2013) 953–966.
[61] P.H. Tobash, S. Bobev, F. Ronning, J.D. Thompson, J.L. Sarrao, J. Alloys Compd. 488 (2009) 511.
[62] W.H. Lee, R.N. Shelton, S.K. Dhar, K.A. Gschneidner Jr., Phys. Rev. B 35 (1987) 8523.
[63] [a] J. Zhang, B. Hmiel, A. Antonelli, P.H. Tobash, S. Bobev, S. Saha, K. Kirshenbaum, R.L. Greene, J. Paglione, J. Solid State Chem. 196 (2012) 586;
[b] A.M. Stewart, B.R. Coles, J. Phys. F, Metal Phys. 4 (1974) 458.